THE JOURNAL OF PHYSICAL CHEMISTRY Letters

Identifying and Rationalizing the Differing Surface Reactions of Low-Energy Electrons and Ions with an Organometallic Precursor

Rachel M. Thorman, Scott J. Matsuda, Lisa McElwee-White, and D. Howard Fairbrother*

Cite This: *J. Phys. Chem. Lett.* 2020, 11, 2006−2013

Read Online

ACCESS | Metrics & More | Article Recommendations | Supporting Information

ABSTRACT: Surface reactions of electrons and ions with physisorbed organometallic precursors are fundamental processes in focused electron and ion beam-induced deposition (FEBID and FIBID, respectively) of metal-containing nanostructures. Markedly different surface reactions occur upon exposure of nanometer-scale films of (η^5-Cp)Fe(CO)$_2$Re(CO)$_5$ to low-energy electrons (500 eV) compared to argon ions (860 eV). Electron-induced surface reactions are initiated by electronic excitation and fragmentation of (η^5-Cp)Fe(CO)$_2$Re(CO)$_5$, causing half of the CO ligands to desorb. Residual CO ligands decompose under further electron irradiation. In contrast, Ar$^+$-induced surface reactions proceed by an ion−molecule momentum/energy transfer process, causing the desorption of all CO ligands without significant ion-induced precursor desorption. This initial decomposition step is followed by ion-induced sputtering of the deposited atoms. The fundamental insights derived from this study can be used not only to rationalize the composition of deposits made by FEBID and FIBID but also to inform the choice of a charged particle deposition strategy and the design of new precursors for these emerging nanofabrication tools.

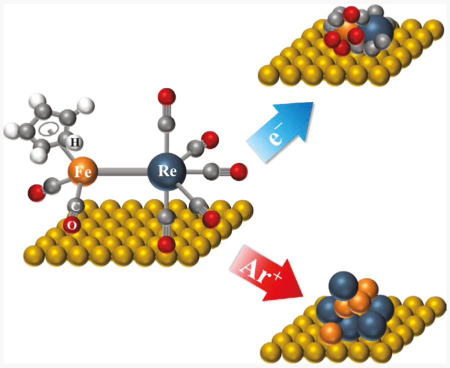

Focused electron beam-induced deposition (FEBID) and focused ion beam-induced deposition (FIBID) are single-step deposition processes in which well-defined three-dimensional nanostructures can be "written" onto planar or nonplanar surfaces with an electron or ion beam "pen".[1−5] In both FEBID and FIBID, a substrate in a high-vacuum system is exposed to a constant flux of a volatile organometallic precursor via a gas inlet system. A high-energy (1−30 kV), tightly focused electron or ion beam impacts the surface, decomposing physisorbed precursor molecules. Nonvolatile metal-containing fragments are deposited onto the substrate, creating metal-containing nanostructures, while volatile fragments/ligands desorb.

In FEBID, deposition is generally understood to be initiated by low-energy electrons (LEEs, <100 eV) generated by the interaction of the primary beam with the substrate.[1,6−8] The initial reaction step involves electron attachment, ionization, or electronic excitation of the precursor and is typically characterized by a degree of ligand loss and the formation of a surface-bound intermediate containing the metal atom and residual ligands.[9−16] Further electron irradiation, however, typically leads to decomposition of the residual ligands rather than further ligand desorption.[11−13,15] An exception to this process occurs when metal−halogen bonds are present, where the halogen atoms can be removed by electron-stimulated desorption.[9,10,17] The second step is typically responsible for the majority of the organic contamination in the final deposit [e.g., W(CO)$_6$].[12]

Far fewer insights into the fundamental bond-breaking processes involved in FIBID have been described. This is in part because a number of different processes can contribute to the initial deposition step in FIBID,[1,18,19] including interactions between the primary ion and the adsorbate and/or reactions between the adsorbate and secondary electrons generated by the impact of the primary ion beam with the substrate. FIBID can also proceed through momentum/energy transfer between the incident ion and the substrate.[18] In the ion-limited regime of FIBID, deposition is limited by the flux of incident ions rather than the coverage of precursor molecules.[1] Ion−molecule interactions are therefore expected to play a particularly important role in this regime, although the interaction of the ion beam with the adsorbate/substrate will also generate secondary electrons and thus electron−molecule interactions may also contribute. The importance of studying ion-induced reactions with adsorbed films of precursor molecules has been further emphasized by a recent report demonstrating the use of cryo-FIBID to grow metallic contacts more than 600 times faster than in conventional FIBID.[20,21]

In this study, we undertake a molecular-level surface science approach to determine and compare the sequence of bond-breaking steps that occur when an organometallic precursor [(η^5-Cp)Fe(CO)$_2$Re(CO)$_5$] is exposed to low-energy (<1 keV) argon ions or electrons. Argon ions were used to eliminate ion

Received: January 7, 2020
Accepted: February 14, 2020
Published: February 14, 2020

https://dx.doi.org/10.1021/acs.jpclett.0c00061

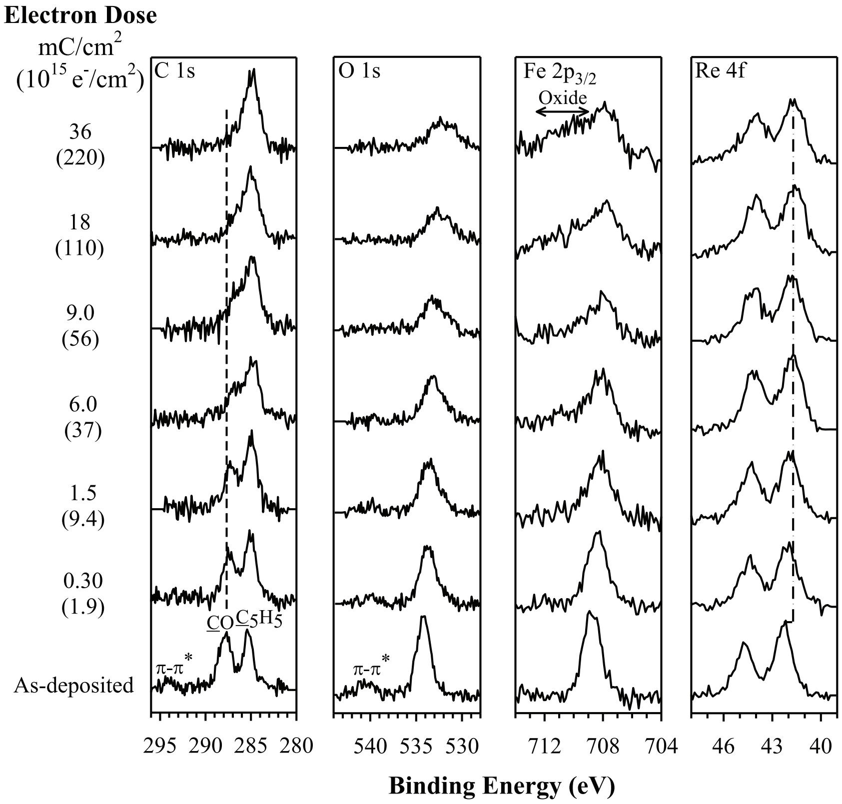

Figure 1. Changes to the C (1s), O (1s), Fe ($2p_{3/2}$), and Re (4f) XPS regions upon 500 eV electron irradiation of ≈1.5−2.0 nm $CpFe(CO)_2Re(CO)_5$ thin films adsorbed on polycrystalline gold substrates at −100 °C, corresponding to approximately 1−2 ML coverage. The bottom spectrum represents the adsorbed ("as-deposited") film prior to electron irradiation. A dashed line in the C (1s) region denotes the binding energy of carbon associated with the carbonyl ligand. The horizontal arrows in the Fe ($2p_{3/2}$) spectrum show the region where oxidized iron is observed. The dashed−dotted line in the Re (4f) region shows the change in binding energies of the Re ($4f_{7/2}$) peak during electron irradiation. The electron dose is shown on the left-hand side expressed in terms of both current density (mC/cm^2) and effective dose (e$^-$/cm^2).

implantation, which was not observed on the Au substrate, and reactions associated with ion fragmentation (e.g., oxidation when using O_2^+). The effects of low-energy electron (500 eV) and Ar$^+$ (860 eV) irradiation on nanometer-scale films of (η^5-Cp)$Fe(CO)_2Re(CO)_5$ have been studied using *in situ* X-ray photoelectron spectroscopy (XPS) to probe changes in bonding and chemical composition and mass spectrometry (MS) to identify volatile species produced during electron/ion exposure.

Figures 1 and 2 contrast the effect of electron and Ar$^+$ irradiation on 1.5−2.0 nm thick (η^5-Cp)$Fe(CO)_2Re(CO)_5$ films, respectively. Analysis of the "as-deposited" films indicates that (η^5-Cp)$Fe(CO)_2Re(CO)_5$ adsorbs molecularly onto the Au substrates at −100 °C (see the Supporting Information for details), while control studies (Figure S1) reveal that (η^5-Cp)$Fe(CO)_2Re(CO)_5$ films were unchanged by X-rays for the irradiation times needed to acquire spectra.

Under the influence of electron irradiation (Figure 1), the carbonyl ($\underline{C}$O) C (1s) peak initially at 287.8 eV decreases in intensity and shifts to a slightly lower binding energy, while the $\underline{C}$O π-to-π* shakeup feature at 294.0 eV disappears. For electron doses of >6.0 mC/cm^2, the $\underline{C}$O peak is observed as a higher-binding energy shoulder to the larger C (1s) peak at 285.3 eV. This larger peak corresponds to CC/CH species, including the carbon atoms in the cyclopentadienyl ligand. For the largest electron doses (36 mC/cm^2), only a single C (1s) peak is observed at 284.9 eV.

In the O (1s) region, a systematic decrease in the O (1s) peak intensity occurs for electron doses of <6.0 mC/cm^2. At larger electron doses, however, the intensity in the O (1s) region remains roughly constant, although the peak shape changes. A lower-binding energy shoulder grows in, culminating in a broad, low-intensity peak centered at ≈532.1 eV, consistent with oxide formation.[11] In the Fe ($2p_{3/2}$) region, the peak position downshifts slightly during the initial stages of electron irradiation, although the most obvious change is the peak broadening to higher binding energies for electron doses of >6.0 mC/cm^2, indicative of iron oxidation.[22] In the Re (4f) region, for electron doses of <6.0 mC/cm^2, the peaks broaden and the Re ($4f_{7/2}$) binding energy decreases from 42.3 to 41.6 eV. For doses of >6.0 mC/cm^2, the Re (4f) peak profile is essentially unchanged. In contrast to the C (1s) and O (1s) regions, changes to the Fe (2p) spectral envelopes and Re (4f) regions occur without measurable changes to metal atom coverage (see Figure 1).

Figure 2 shows that the effect of Ar$^+$ bombardment on adsorbed (η^5-Cp)$Fe(CO)_2Re(CO)_5$ molecules differs significantly from the effect of electron irradiation. In the C (1s) region, the $\underline{C}$O peak decreases in intensity and has disappeared after ~0.048 mC/cm^2 of Ar$^+$ exposure. During this same period of Ar$^+$ bombardment, the cyclopentadienyl C (1s) peak at 285.3 eV broadens, becoming an asymmetric peak centered at ≈284.1 eV with an intensity that was ≈80% of that of the initial cyclopentadienyl C (1s) peak area. For Ar$^+$ exposures of >0.048 mC/cm^2, the intensity of this peak begins to decrease until no carbon atoms remain after 0.28 mC/cm^2 of Ar$^+$ bombardment. Changes in the O (1s) region are even more distinct from those

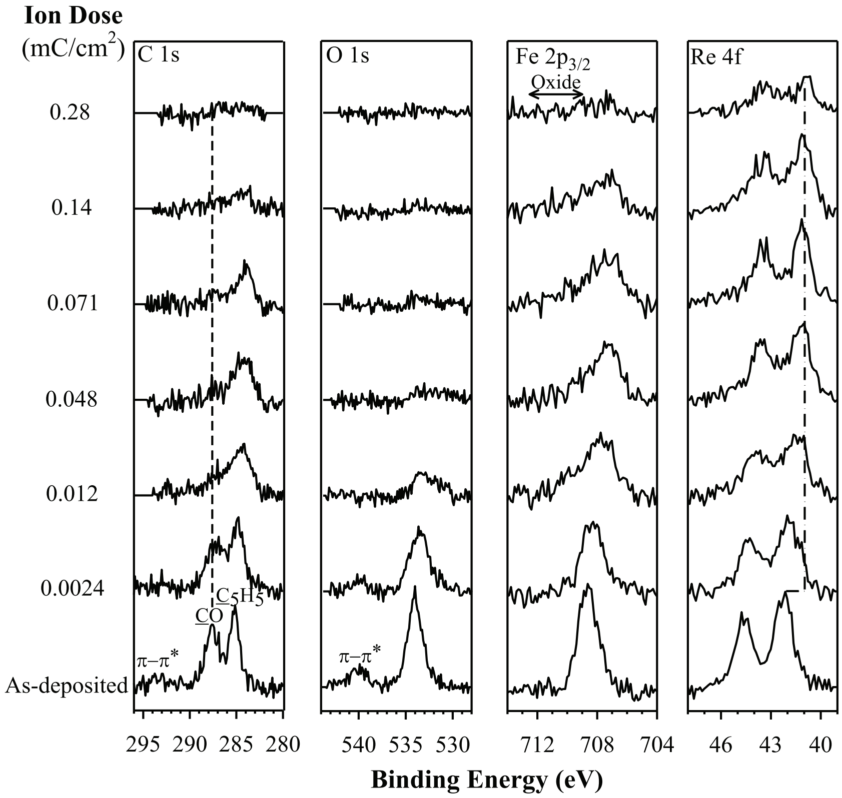

Figure 2. Evolution of C (1s), O (1s), Fe ($2p_{3/2}$), and Re (4f) XPS regions upon 860 eV Ar^+ bombardment of ≈1.3−1.8 nm thin films of $CpFe(CO)_2Re(CO)_5$, corresponding to approximately 1−2 ML coverage. The bottom spectrum represents the adsorbed film prior to argon ion bombardment. The dashed vertical line in the C (1s) region denotes the binding energy of carbon atoms associated with carbonyl ligands. Arrows in the top Fe ($2p_{3/2}$) spectrum show the region in which iron oxidation would be expected. The dashed−dotted line in the Re (4f) region shows the shift in the binding energy of the Re ($4f_{7/2}$) peak. The argon ion dose is reported on the left-hand side in current density (mC/cm^2).

due to electron irradiation. Notably, Ar^+ bombardment leads to a rapid decrease in the coverage of oxygen atoms; after 0.048 mC/cm^2 of Ar^+ exposure, no oxygen atoms remain. Changes to the Fe ($2p_{3/2}$) region are characterized by peak broadening, a noticeable decrease in binding energy (from 708.7 to 707.2 eV after 0.14 mC/cm^2), and a steady decrease in overall signal intensity, albeit at a slower rate than in the O (1s) region. After 0.28 mC/cm^2 of Ar^+ exposure, virtually all of the iron has been removed. In contrast to electron irradiation (Figure 1), no iron oxide shoulder is observed in the Fe ($2p_{3/2}$) region between 709 and 711 eV. Analogous to the Fe ($2p_{3/2}$) region, the Re (4f) doublet also broadens and shifts to a lower binding energy upon Ar^+ bombardment. The Re (4f) signal intensity also decreases, although a measurable Re atom coverage still remains after 0.28 mC/cm^2 of Ar^+ bombardment.

Electron Irradiation. The electron beam-induced reactions of (η^5-Cp)$Fe(CO)_2Re(CO)_5$ occur in two sequential steps: the first taking place at electron doses of ≤6.0 mC/cm^2 and the second at doses of ≥6.0 mC/cm^2. This can be seen in Figure 3, which shows the effect of electron and ion beam irradiation on the fractional coverage of oxygen, carbon, and rhenium atoms, and Figure 4, which shows the corresponding changes in binding energies of the Re ($4f_{7/2}$) and Fe ($2p_{3/2}$) peaks. Electron doses of <6.0 mC/cm^2, shown as the blue shaded region, produce an exponential loss of the relative coverage of oxygen and carbon (Figure 3) along with a concomitant decrease in the binding energies of the Fe ($2p_{3/2}$) and Re (4f) peaks (Figure 4). For electron doses of ≥6.0 mC/cm^2, each of these parameters remains constant. These initial changes in the XPS spectra are caused by electron-stimulated decomposition of the precursor, which leads to CO desorption as observed directly by MS (Figure 5 and Figure S2). On the basis of the fractional decreases in the O (1s) regions, we can conclude that about half (three or four) of the CO ligands in the precursor desorb as a consequence of electron-stimulated decomposition (Figure S3). The decrease in the Fe ($2p_{3/2}$) and Re ($4f_{7/2}$) binding energies during this same period of electron irradiation (Figures 1 and 4) is a consequence of precursor decomposition/decarbonylation. Analysis of Figures 1 and 3 demonstrates that all of the carbon atoms in the Cp ligand remain.[9,11] While the presence or absence of H cannot be detected with XPS, previous studies have demonstrated electron-stimulated C−H bond cleavage in adsorbed organic molecules.[23−26] We can therefore reasonably assume that the Cp ligand decomposes:

$$C_5H_{5(ads)} + e^- \rightarrow 5C_{(ads)} + 5/2H_{2(g)}\uparrow \quad (1a)$$

The initial precursor decomposition/deposition step can therefore be summarized as

$$CpFe(CO)_2Re(CO)_{5(ads)} + e^- \rightarrow C_5FeRe(CO)_{(7-n)(ads)} + nCO(g)\uparrow + 5/2H_{2(g)}\uparrow \ (n = 3\text{–}4) \quad (1b)$$

This reaction step is illustrated in Figure 6 (top), with the product best viewed as a partially decarbonylated intermediate.[9,11−13,16] On the basis of previous studies, the desorption of multiple CO ligands suggests that precursor decomposition is a consequence of dissociative ionization;[27,28] however, this cannot be conclusively determined. This hypothesis is supported by MS

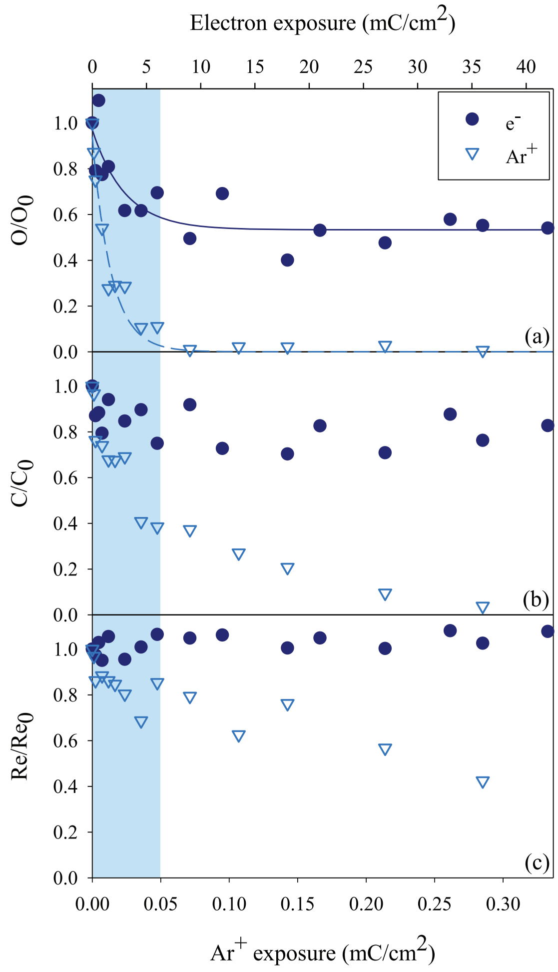

Figure 3. Changes in the fractional coverage of (a) oxygen, (b) carbon, and (c) rhenium atoms upon electron (dark circles, top x axis) and argon ion (light empty triangles, bottom x axis) exposure. The changes in composition that occur during the initial region of electron (~6.0 mC/cm^2) or argon ion (~0.048 mC/cm^2) exposure are denoted by the blue shaded region. The decay in the fractional coverage of oxygen atoms by electron (dark solid line) and argon ion (light dashed line) exposure has been fit using an exponential decay profile of $(O_j/O_0) = Ae^{-bj} + c$, where j is the total electron or argon ion exposure, (O_j/O_0) is the fractional coverage of oxygen atoms, and A, b, and c are constants.

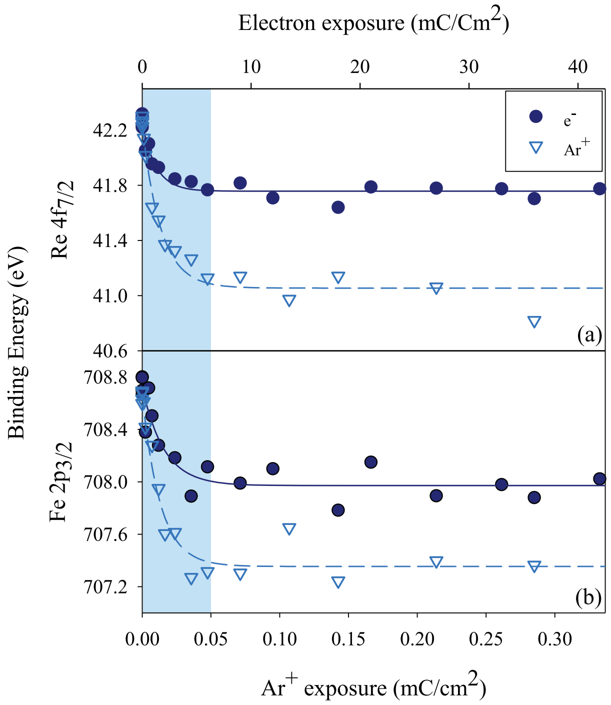

Figure 4. Changes in the binding energies of the (a) Re ($4f_{7/2}$) peak and (b) Fe ($2p_{3/2}$) peak upon electron (dark circles, top x axis) and argon ion (empty triangles, bottom x axis) exposure. The initial ≈6.0 mC/cm^2 of electron exposure and 0.048 mC/cm^2 of argon ion exposure are denoted by the blue shaded region. The shift in peak positions by electron (dark solid line) and argon ion (light dashed line) exposure has been fit using exponential decay profiles of the form $y_j = Ae^{-bj} + c$, where y_j is the binding energy at electron or argon ion exposure j and c is the binding energy at the end of the exposure.

data of gas phase (η^5-Cp)Fe(CO)$_2$Re(CO)$_5$ (Figure S4), which shows that 70 eV electron bombardment also leads principally to fragments formed by multiple CO ligand loss.

For electron doses of ≥6.0 mC/cm^2, the XPS data (Figures 1, 3, and 4) show that no further carbon or oxygen desorbs and the Fe ($2p_{3/2}$) and Re (4f) binding energies remain unchanged. However, changes in the C (1s) and O (1s) spectral envelopes indicate that the CO ligands in the partially decarbonylated intermediate described in eq 1b decompose under the influence of continued electron irradiation. In the C (1s) region, the high-binding energy shoulder associated with the residual CO groups disappears while the intensity of the principal carbon peak at 284.9 eV associated with C−C/C−H species increases. In the O (1s) region, the appearance of a lower-binding energy O (1s) shoulder and the growth of the higher-binding energy Fe ($2p_{3/2}$) shoulder indicate iron oxidation. Thus, electron-stimulated decomposition of these residual CO ligands produces graphitic carbon and reactive oxygen species (ROS) that oxidize iron:

$$CO_{(ads)} + e^- \rightarrow C_{(ads)} + ROS \tag{2a}$$

$$ROS + Fe_{(ads)} \rightarrow Fe_xO_{y(ads)} \tag{2b}$$

The sequence of electron-induced reactions shown in Figure 6 (top) is similar to the electron-stimulated reactions reported for other carbonyl-containing organometallics.[11−13,15] The incomplete desorption of the CO ligands from (η^5-Cp)Fe(CO)$_2$Re(CO)$_5$ also provides a rationale for the poor fit between the CO desorption rate and the oxygen coverage determined by XPS (Figure 5). However, we can reanalyze the CO desorption data, adding an offset (determined by XPS) to reflect the observation that only some of the oxygen atoms/CO ligands desorb. The rate of CO desorption is now well correlated with the fractional loss of oxygen that occurs during the electron-stimulated decomposition of the precursor (Figure S5).

Ion Bombardment. Analysis of Figures 2 and 3 shows that ion-induced reactions with (η^5-Cp)Fe(CO)$_2$Re(CO)$_5$ also occur in two regimes, the first of which is indicated by the shaded blue region in Figures 3 and 4. In this initial ≈0.048 mC/cm^2 of ion bombardment, some ion-induced precursor desorption may occur as demonstrated by the ≈20% decrease in the intensity of the Re signal, but the much more significant changes in the C (1s) and O (1s) regions indicate that this initial phase is dominated by ion-induced reactions with the organometallic precursor. Most significantly, Figure 2 shows that ≈0.048 mC/cm^2 of Ar$^+$ exposure completely removes all intensity in the O (1s) region, as well as all C (1s) intensity at 287.8 eV associated with the carbonyl ligand, suggesting that all carbonyl ligands

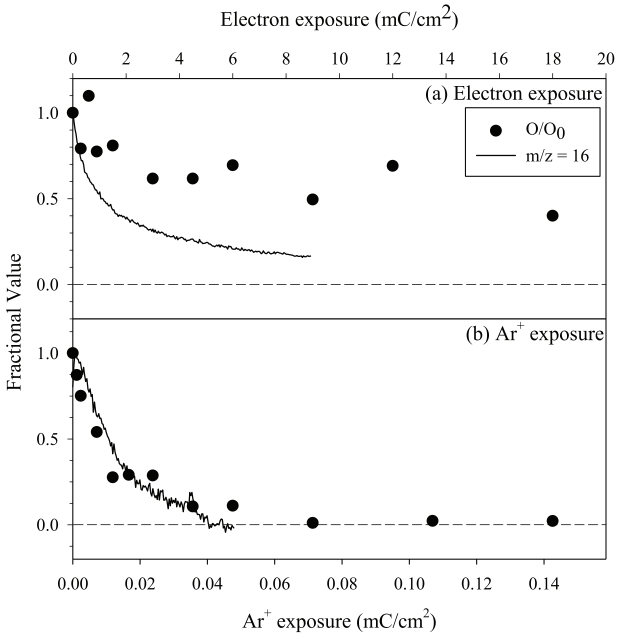

Figure 5. Kinetics of gas phase CO evolution from ≈1.5−2.0 nm thin films of adsorbed $CpFe(CO)_2Re(CO)_5$ upon (a) 500 eV electron irradiation (top x axis) and (b) 860 eV Ar^+ bombardment (bottom x axis) as measured by the O (m/z 16) peak (solid black line). For both electron and ion exposure, the normalized O signal observed by mass spectrometry is overlaid with the concurrent change in the fractional oxygen coverage as measured by the O (1s) XPS signal (filled black circles). The O signal was chosen over the more intense m/z 28 signal to avoid potential contamination from other species (e.g., N_2) at m/z 28. The C signal (m/z 12) exhibited the same decay profile as the O (m/z 16) signal (Figure S3), showing that both fragments originate exclusively from CO.

have desorbed. This assertion is supported by the correlation between the CO desorption rate observed by MS and the fractional CO coverage on the surface determined by the O (1s) XPS area (Figure 5). Figures 2 and 4 also show that both the Fe ($2p_{3/2}$) and Re (4f) peaks decrease in binding energy as all of the CO ligands desorb to values proximate to those of the pure metals.[29−31] In comparison, the decrease in the Fe ($2p_{3/2}$) and Re (4f) peak positions during electron exposure is roughly half of that from ion exposure, likely a consequence of the incomplete CO desorption during electron exposure. At this stage of the Ar^+-induced reaction sequence, when all CO ligands have desorbed from the $(\eta^5\text{-Cp})Fe(CO)_2Re(CO)_5$ molecules, ≈40% of the initial carbon remains (Figure 3), consistent with the remaining carbon being derived from the cyclopentadienyl ring. On the basis of previous studies of molecular ion-induced reactions with hydrocarbons[32] and the significant broadening of the C (1s) peak, we believe that the cyclopentadienyl ligand is dehydrogenated during this period. Therefore, in addition to a small amount of ion-induced sputtering/desorption, the initial ion-induced reactions can be summarized by eq 3 and Figure 6 (bottom):

$$\begin{aligned}&CpFe(CO)_2Re(CO)_{5(ads)} + Ar^+_{(g)}\ (800\ eV)\\&\rightarrow C_5FeRe_{(ads)} + 7CO_{(g)}\uparrow +5/2H_{2(g)}\uparrow\end{aligned} \qquad (3)$$

Thus, while all of the carbonyl ligands desorb, no cyclopentadienyl carbon atoms are removed from the surface. More sustained Ar^+ bombardment (>0.048 mC/cm^2) causes ion-induced physical sputtering, as shown in Figure 6 (bottom). This is evidenced by decreases in intensities within the C (1s), Fe ($2p_{3/2}$), and Re (4f) regions (Figures 2 and 3).

In our experiment, the low energy (860 eV) and ion flux (measured target current of less than −100 nA/cm^2; calculated ion current of ~40 nA/cm^2) are likely to limit any processes initiated by surface activation, including thermal effects. Indeed, we did not observe any increase in substrate temperature during ion exposure, even when the ion beam was incident upon the thermocouple attached to the backside of the sample holder. Consequently, our results are a consequence of low-energy ion−molecule and/or electron−molecule interactions.

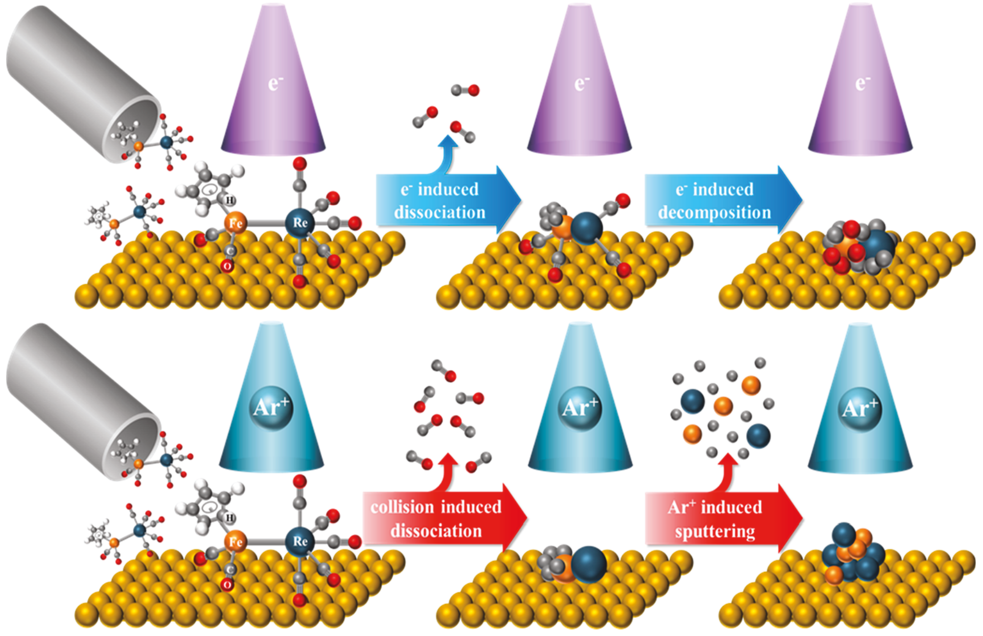

Figure 6. Schematic representation of the sequence of molecular-level events that accompany the 500 eV electron (top) and 860 eV Ar^+ ion (bottom) exposure of adsorbed $CpFe(CO)_2Re(CO)_5$ on a gold substrate.

Upon comparison of the effects of low-energy electron and Ar^+ exposure, it is evident that the two processes are mechanistically different. Electron-induced reactions of (η^5-Cp)$Fe(CO)_2Re(CO)_5$ are characterized by desorption of only half of the CO ligands (eq 1b) followed by decomposition of the residual CO ligands (eq 2a). In contrast, all CO ligands desorb during ion beam exposure (eq 3) followed by physical sputtering of the remaining atoms. These differences support the hypothesis that direct ion-induced reactions of (η^5-Cp)$Fe(CO)_2Re(CO)_5$ are dominated by ion−molecule interactions, rather than reactions between the adsorbate and low-energy secondary electrons generated by the interactions of the primary ion beam with the substrate.

In direct ion−molecule interactions, a significant amount of energy will be transferred during the collision of the 860 eV Ar^+ and the adsorbed (stationary) (η^5-Cp)$Fe(CO)_2Re(CO)_5$ molecules. If this interaction is modeled as a simple head-on collision between an incident ion and an adsorbed precursor,[18] then the maximum energy (ΔK) that can be transferred assuming a perfectly elastic collision with impact parameter $b \approx 0$ is

$$\Delta K = K \times 4m_{\mathrm{ion}}m_{\mathrm{mol}}/(m_{\mathrm{ion}} + m_{\mathrm{mol}})^2 \qquad (4)$$

where K is the kinetic energy of the incident ion, m_{ion} is the mass of the ion, and m_{mol} is the mass of the adsorbed molecule. Using this equation for an 860 eV incident Ar^+, the maximum energy that can be transferred to (η^5-Cp)$Fe(CO)_2Re(CO)_5$ is calculated as 235 eV. In reality, the energy transferred will depend on the impact parameter and thus fall between 0 and 218.3 eV. Typically, M−CO ligands have bond dissociation energies (BDEs) of 1−2 eV.[33−38] It is thus apparent that, for the vast majority of the collisions, the energy transferred will be well in excess of that required to dissociate all of the M−CO ligands. The MS data (Figure S2) show that CO desorbs once it has been generated. We postulate that for the CO ligands, energy transfer leads to M−CO dissociation rather than C≡O dissociation because of the significant disparity in the energy required for M−CO dissociation (<2 eV) compared to that required for C≡O dissociation (BDE = 11.16 eV).[39]

The η^5-cyclopentadienyl ligand has a M−L BDE slightly higher than that of the CO ligands (the first Fe−Cp BDE in ferrocene is 4 eV, while the second is 2.2 eV),[40] while the C−C and C−H bonds have BDEs of ≈5 eV.[41,42] It is thus likely that the energy transferred during the ion−precursor collision will lead to a mixture of ligand dissociation and decomposition. Although our experimental data do not allow determination of the detailed fate of the Cp ligand, it is apparent that any Fe−Cp bond dissociation does not lead to Cp desorption as the carbon atoms associated with it remain on the surface during this initial period (Figures 2 and 3) and its desorption from the surface via MS is not evident (Figure S2). On Cu(100), cyclopentadienyl has been shown to be stable up to 600 K due to strong chemisorption;[43] it is therefore possible that any intact Cp ligands dissociated from Fe during precursor decomposition will similarly remain on the surface and be decomposed by subsequent ion bombardment as hypothesized in eq 3. Interestingly, despite the large quantity of energy transferred to (η^5-Cp)$Fe(CO)_2Re(CO)_5$ upon Ar^+ impact, bond dissociation within the precursor rather than molecular desorption dominates, even though the molecules are only physisorbed.

Our results can also be compared to those of previous studies of ion-induced reactions with adsorbed molecules and thin films. For example, physical sputtering of CO and NH_3 was dominant during 10−1000 eV Xe^+ and SF_5^+ bombardment of CO or NH_3 adsorbed on Ni(111).[44] This is consistent with our observation of CO desorption predominating over CO decomposition. In related studies, the modification of alkanethiolate self-assembled monolayers by organic ions was independent of the chemical ion and consistent with momentum transfer,[32] analogous to the mechanism proposed in this study and similar to models used to explain surface-induced dissociation.[45]

This study reveals for the first time how a surface science approach can elucidate and compare the sequence of elementary steps involved in FEBID and FIBID of metal-containing nanostructures, including reactions of different ligands. In FEBID, this involves a two-step process characterized by initial ligand desorption mediated by electronic excitation and decomposition of the precursor, typically followed by ligand decomposition as seen for (η^5-Cp)$Fe(CO)_2Re(CO)_5$ and other precursors.[11−15] In contrast, FIBID is found to be initiated by a transfer of energy between the incident ion and the stationary adsorbate, which in the case of (η^5-Cp)$Fe(CO)_2Re(CO)_5$ leads to complete CO desorption. The residual carbon atoms associated with the Cp ligand are subsequently removed by physical sputtering, along with the Fe and Re atoms. In FEBID, this type of fundamental information has already been used to rationalize the composition of deposits and to develop new precursors for FEBID [e.g., $Pt(CO)_2Cl_2$].[10,17] Data from this study indicate that deposits created by FIBID using (η^5-Cp)$Fe(CO)_2Re(CO)_5$ will be devoid of CO and it would be possible to create deposits containing only Fe and Re atoms by tuning the ion and precursor flux. Our results also suggest that the momentum transfer process underlying deposition in low-energy FIBID in the ion-limited regime will lead to complete or nearly complete carbonyl removal for some metal carbonyls, a process typically not found in FEBID.[46] Low-energy ion-induced deposition using inert ions and metal carbonyl precursors could thus provide a route to produce deposits with extremely high metal contents,[47] although the deposit composition will also depend on the balance between precursor and ion flux.

■ ASSOCIATED CONTENT

SI Supporting Information

The Supporting Information is available free of charge at https://pubs.acs.org/doi/10.1021/acs.jpclett.0c00061.

Experimental methods, control studies, precursor synthesis, and characterization (PDF)

■ AUTHOR INFORMATION

Corresponding Authors

Rachel M. Thorman − *Department of Chemistry, Johns Hopkins University, Baltimore, Maryland 21218-2685, United States*

Scott J. Matsuda − *Department of Chemistry, University of Florida, Gainesville, Florida 32611-7200, United States*

Lisa McElwee-White − *Department of Chemistry, University of Florida, Gainesville, Florida 32611-7200, United States;* orcid.org/0000-0001-5791-5146

D. Howard Fairbrother − *Department of Chemistry, Johns Hopkins University, Baltimore, Maryland 21218-2685, United States;* orcid.org/0000-0003-4405-9728; Email: howardf@jhu.edu

Complete contact information is available at: https://pubs.acs.org/10.1021/acs.jpclett.0c00061

Notes

The authors declare no competing financial interest.

■ ACKNOWLEDGMENTS

L.M.-W. and D.H.F. thank the National Science Foundation for support of this work through the linked collaborative grants CHE-1607621, CHE-1904559, CHE-1607547, and CHE-1904802. Support of mass spectrometry instrumentation at the University of Florida was provided by the National Institutes of Health through Grant S10 OD021758-01A1.

■ REFERENCES

(1) Utke, I.; Hoffmann, P.; Melngailis, J. Gas-Assisted Focused Electron Beam and Ion Beam Processing and Fabrication. *J. Vac. Sci. Technol. B Microelectron. Nanom. Struct.* **2008**, *26* (4), 1197.

(2) Melngailis, J. Focused Ion Beam Technology and Applications. *J. Vac. Sci. Technol., B: Microelectron. Process. Phenom.* **1987**, *5* (2), 469.

(3) Utke, I.; Gölzhäuser, A. Small, Minimally Invasive, Direct: Electrons Induce Local Reactions of Adsorbed Functional Molecules on the Nanoscale. *Angew. Chem., Int. Ed.* **2010**, *49* (49), 9328−9330.

(4) Córdoba, R.; Mailly, D.; Rezaev, R. O.; Smirnova, E. I.; Schmidt, O. G.; Fomin, V. M.; Zeitler, U.; Guillamón, I.; Suderow, H.; De Teresa, J. M. Three-Dimensional Superconducting Nanohelices Grown by He^+-Focused-Ion-Beam Direct Writing. *Nano Lett.* **2019**, *19* (12), 8597−8604.

(5) Winkler, R.; Fowlkes, J. D.; Rack, P. D.; Plank, H. 3D Nanoprinting via Focused Electron Beams. *J. Appl. Phys.* **2019**, *125* (21), 210901.

(6) Thorman, R. M.; T P, R. K.; Fairbrother, D. H.; Ingólfsson, O. The Role of Low-Energy Electrons in Focused Electron Beam Induced Deposition: Four Case Studies of Representative Precursors. *Beilstein J. Nanotechnol.* **2015**, *6* (1), 1904−1926.

(7) van Dorp, W. F.; Hagen, C. W. A Critical Literature Review of Focused Electron Beam Induced Deposition. *J. Appl. Phys.* **2008**, *104* (8), 081301.

(8) Böhler, E.; Warneke, J.; Swiderek, P. Control of Chemical Reactions and Synthesis by Low-Energy Electrons. *Chem. Soc. Rev.* **2013**, *42* (24), 9219−9231.

(9) Spencer, J. A.; Brannaka, J. A.; Barclay, M.; McElwee-White, L.; Fairbrother, D. H. Electron-Induced Surface Reactions of η^3-Allyl Ruthenium Tricarbonyl Bromide $[(\eta^3\text{-}C_3H_5)Ru(CO)_3Br]$: Contrasting the Behavior of Different Ligands. *J. Phys. Chem. C* **2015**, *119* (27), 15349−15359.

(10) Spencer, J. A.; Wu, Y.-C.; McElwee-White, L.; Fairbrother, D. H. Electron Induced Surface Reactions of *cis*-$Pt(CO)_2Cl_2$: A Route to Focused Electron Beam Induced Deposition of Pure Pt Nanostructures. *J. Am. Chem. Soc.* **2016**, *138* (29), 9172−9182.

(11) Unlu, I.; Spencer, J. A.; Johnson, K. R.; Thorman, R. M.; Ingólfsson, O.; McElwee-White, L.; Fairbrother, D. H. Electron Induced Surface Reactions of $(\eta^5\text{-}C_5H_5)Fe(CO)_2Mn(CO)_5$, a Potential Heterobimetallic Precursor for Focused Electron Beam Induced Deposition (FEBID). *Phys. Chem. Chem. Phys.* **2018**, *20* (11), 7862−7874.

(12) Rosenberg, S. G.; Barclay, M.; Fairbrother, D. H. Electron Induced Reactions of Surface Adsorbed Tungsten Hexacarbonyl ($W(CO)_6$). *Phys. Chem. Chem. Phys.* **2013**, *15* (11), 4002−4015.

(13) Rosenberg, S. G.; Barclay, M.; Fairbrother, D. H. Electron Beam Induced Reactions of Adsorbed Cobalt Tricarbonyl Nitrosyl ($Co(CO)_3NO$) Molecules. *J. Phys. Chem. C* **2013**, *117* (31), 16053−16064.

(14) Landheer, K.; Rosenberg, S. G.; Bernau, L.; Swiderek, P.; Utke, I.; Hagen, C. W.; Fairbrother, D. H. Low-Energy Electron-Induced Decomposition and Reactions of Adsorbed Tetrakis(Trifluorophosphine)Platinum $[Pt(PF_3)_4]$. *J. Phys. Chem. C* **2011**, *115* (35), 17452−17463.

(15) T P, R. K.; Unlu, I.; Barth, S.; Ingólfsson, O.; Fairbrother, D. H. Electron Induced Surface Reactions of $HFeCo_3(CO)_{12}$, a Bimetallic Precursor for Focused Electron Beam Induced Deposition (FEBID). *J. Phys. Chem. C* **2018**, *122* (5), 2648−2660.

(16) T P, R. K.; Weirich, P.; Hrachowina, L.; Hanefeld, M.; Bjornsson, R.; Hrodmarsson, H. R.; Barth, S.; Fairbrother, D. H.; Huth, M.; Ingólfsson, O. Electron Interactions with the Heteronuclear Carbonyl Precursor $H_2FeRu_3(CO)_{13}$ and Comparison with $HFeCo_3(CO)_{12}$: From Fundamental Gas Phase and Surface Science Studies to Focused Electron Beam Induced Deposition. *Beilstein J. Nanotechnol.* **2018**, *9* (1), 555−579.

(17) Spencer, J. A.; Barclay, M.; Gallagher, M. J.; Winkler, R.; Unlu, I.; Wu, Y.-C.; Plank, H.; McElwee-White, L.; Fairbrother, D. H. Comparing Postdeposition Reactions of Electrons and Radicals with Pt Nanostructures Created by Focused Electron Beam Induced Deposition. *Beilstein J. Nanotechnol.* **2017**, *8* (1), 2410−2424.

(18) Dubner, A. D.; Wagner, A.; Melngailis, J.; Thompson, C. V. The Role of the Ion-solid Interaction in Ion-beam-induced Deposition of Gold. *J. Appl. Phys.* **1991**, *70* (2), 665−673.

(19) Chen, P.; Salemink, H. W. M.; Alkemade, P. F. A. Roles of Secondary Electrons and Sputtered Atoms in Ion-Beam-Induced Deposition. *J. Vac. Sci. Technol. B Microelectron. Nanom. Struct.* **2009**, *27* (6), 2718.

(20) Córdoba, R.; Orús, P.; Strohauer, S.; Torres, T. E.; De Teresa, J. M. Ultra-Fast Direct Growth of Metallic Micro- and Nano-Structures by Focused Ion Beam Irradiation. *Sci. Rep.* **2019**, *9* (1), 14076.

(21) De Teresa, J.; Orús, P.; Córdoba, R.; Philipp, P. Comparison between Focused Electron/Ion Beam-Induced Deposition at Room Temperature and under Cryogenic Conditions. *Micromachines* **2019**, *10* (12), 799.

(22) Mansour, A. N.; Brizzolara, R. A. Characterization of the Surface of FeO Powder by XPS. *Surf. Sci. Spectra* **1996**, *4* (4), 345−350.

(23) Huels, M. A.; Dugal, P.-C.; Sanche, L. Degradation of Functionalized Alkanethiolate Monolayers by 0−18 eV Electrons. *J. Chem. Phys.* **2003**, *118* (24), 11168−11178.

(24) Olsen, C.; Rowntree, P. A. Bond-Selective Dissociation of Alkanethiol Based Self-Assembled Monolayers Adsorbed on Gold Substrates, Using Low-Energy Electron Beams. *J. Chem. Phys.* **1998**, *108* (9), 3750−3764.

(25) Rowntree, P.; Dugal, P.-C.; Hunting, D.; Sanche, L. Electron Stimulated Desorption of H_2 from Chemisorbed Molecular Monolayers. *J. Phys. Chem.* **1996**, *100* (11), 4546−4550.

(26) Rowntree, P. A. The Use of Highly Organized Molecular Films as Electron Scattering Targets: Spectroscopic and Desorption Measurements of Selective Bond Rupture in Organic Films. *Surf. Sci.* **1997**, *390* (1−3), 70−78.

(27) Thorman, R. M.; Unlu, I.; Johnson, K.; Bjornsson, R.; McElwee-White, L.; Fairbrother, D. H.; Ingólfsson, O. Low Energy Electron-Induced Decomposition of $(\eta^5\text{-}Cp)Fe(CO)_2Mn(CO)_5$, a Potential Bimetallic Precursor for Focused Electron Beam Induced Deposition of Alloy Structures. *Phys. Chem. Chem. Phys.* **2018**, *20* (8), 5644−5656.

(28) Engmann, S.; Stano, M.; Papp, P.; Brunger, M. J.; Matejčík, Š.; Ingólfsson, O. Absolute Cross Sections for Dissociative Electron Attachment and Dissociative Ionization of Cobalt Tricarbonyl Nitrosyl in the Energy Range from 0 to 140 eV. *J. Chem. Phys.* **2013**, *138* (4), 044305.

(29) Zaera, F. A Kinetic Study of the Chemical Vapor Deposition of Iron Films Using Iron Pentacarbonyl. *Langmuir* **1991**, *7* (6), 1188−1191.

(30) Okal, J.; Tylus, W.; Kępiński, L. XPS Study of Oxidation of Rhenium Metal on $\gamma\text{-}Al_2O_3$ Support. *J. Catal.* **2004**, *225* (2), 498−509.

(31) Cimino, A.; De Angelis, B. A.; Gazzoli, D.; Valigi, M. Photoelectron Spectroscopy (XPS) and Thermogravimetry (TG) of Pure and Supported Rhenium Oxides 1. Pure Rhenium Compounds. *Z. Anorg. Allg. Chem.* **1980**, *460* (1), 86−98.

(32) Burroughs, J. A.; Hanley, L. Molecular Ion Modification of a Hexanethiolate Self-Assembled Monolayer during Surface-Induced Dissociation. *Anal. Chem.* **1994**, *66* (21), 3644−3650.

(33) Brown, D. A.; Lyons, H. J.; Sane, R. T. Solvent and Structural Effects in Substitution Reactions of Metal Carbonyl Halides. *Inorg. Chim. Acta* **1970**, *4*, 621−625.

(34) Brown, D. A.; Lyons, H. J.; Manning, A. R.; Rowley, J. M. Kinetics of Substitution Reactions of Cyclopentadienyl Metal Carbonyl Halides. *Inorg. Chim. Acta* **1969**, *3*, 346−350.

(35) Bruce, M. I. Electron-Impact Studies of Organometallic Molecules. Part III. Some Carbonylmetal Halides and Cyclopentadienyls. *Int. J. Mass Spectrom. Ion Phys.* **1968**, *1* (2), 157−190.

(36) Jones, D. J.; Mawby, R. J. Substitution Reactions of Indenyl and Tetrahydroindenyl Iron Carbonyl Complexes: A Kinetic Study. *Inorg. Chim. Acta* **1972**, *6*, 157−160.

(37) Sunderlin, L. S.; Squires, R. R. Bond Strengths in Cyclopentadienyl Metal Carbonyl Anions. *Int. J. Mass Spectrom.* **1999**, *182*−*183*, 149−161.

(38) Diefenbach, A.; Bickelhaupt, F. M.; Frenking, G. The Nature of the Transition Metal-Carbonyl Bond and the Question about the Valence Orbitals of Transition Metals. A Bond-Energy Decomposition Analysis of $TM(CO)_6(q)$ ($TM(q) = Hf^{2-}$, Ta^-, W, Re^+, Os^{2+}, Ir^{3+}). *J. Am. Chem. Soc.* **2000**, *122* (27), 6449−6458.

(39) Dean, J. A. *Lange's Handbook of Chemistry*, 15th ed.; McGraw-Hill: New York, 1999.

(40) Lewis, K. E.; Smith, G. P. Bond Dissociation Energies in Ferrocene. *J. Am. Chem. Soc.* **1984**, *106* (16), 4650−4651.

(41) Speetzen, B.; Kass, S. R. Ferrocene Acidity and C−H Bond Dissociation Energy via Experiment and Theory. *J. Phys. Chem. A* **2019**, *123* (28), 6016−6021.

(42) Fliszár, S. *Atomic Charges, Bond Properties, and Molecular Energies*; John Wiley & Sons, Inc.: Hoboken, NJ, 2008.

(43) Sun, D.-H.; Bent, B. E.; Chen, J. G. Chemistry of Cyclopentadiene on a Cu(100) Surface: Detection of Cyclopentadienyl (C_5H_5) Species as Reaction Intermediates. *J. Vac. Sci. Technol., A* **1997**, *15* (3), 1581−1585.

(44) Ada, E. T.; Hanley, L. Comparing Hyperthermal Molecular and Atomic Ion Sputtering of Adsorbates: Xe^+ versus SF_5^+ on NH_3/CO/Ni(111). *Int. J. Mass Spectrom. Ion Processes* **1998**, *174* (1−3), 231−244.

(45) Williams, E. R.; Jones, G. C.; Fang, L.; Zare, R. N.; Garrison, B. J.; Brenner, D. W. Ion Pickup of Large, Surface-Adsorbed Molecules: A Demonstration of the Eley-Rideal Mechanism. *J. Am. Chem. Soc.* **1992**, *114* (9), 3207−3210.

(46) Porrati, F.; Sachser, R.; Huth, M. The Transient Electrical Conductivity of W-Based Electron-Beam-Induced Deposits during Growth, Irradiation and Exposure to Air. *Nanotechnology* **2009**, *20*, 195301.

(47) Wu, H.; Stern, L. A.; Xia, D.; Ferranti, D.; Thompson, B.; Klein, K. L.; Gonzalez, C. M.; Rack, P. D. Focused Helium Ion Beam Deposited Low Resistivity Cobalt Metal Lines with 10 nm Resolution: Implications for Advanced Circuit Editing. *J. Mater. Sci.: Mater. Electron.* **2014**, *25* (2), 587−595.